J Mater Sci (2021) 56:9254–9262

Electronic materials

Effect of pre-existing nuclei on microstructure and magnetic properties of high B_s FINEMET-like nanocrystalline alloys

Fushan Bai[1,2], Yaqiang Dong[1,3,*], Lei Xie[1], Qiang Li[1,*], Aina He[2,3], Xingjie Jia[2], Jiawei Li[2,3], and Xinmin Wang[2]

[1] School of Physics Science and Technology, Xinjiang University, Urumqi 830046, Xinjiang, China
[2] Zhejiang Province Key Laboratory of Magnetic Materials and Application Technology, CAS Key Laboratory of Magnetic Materials and Devices, Ningbo Institute of Materials Technology and Engineering, Chinese Academy of Sciences, Ningbo 315201, Zhejiang, China
[3] University of Chinese Academy of Sciences, Beijing 100049, China

Received: 29 December 2020
Accepted: 31 January 2021
Published online: 16 February 2021

ABSTRACT

The effect of conventional annealing and rapid annealing on the magnetic properties and microstructure of $Fe_{78+2x}Si_{7.2-x}B_{13-x}Cu_{0.8}Nb_1$ (x = 0, 1, 2) alloys is discussed systematically. The study was found that the existence of a large number of pre-existing nuclei in the amorphous phase of $Fe_{82}Si_{5.2}B_{11}Cu_{0.8}Nb_1$ alloy can produce tiny nanocrystals and thus result in excellent soft magnetic properties. When the average nanocrystal size is 16 nm using rapid annealing, the best soft magnetic performance can be obtained, in which B_s reaches 1.80 T, H_c is 5 A/m, and μ is 20,000 at 1 kHz. The crystallization kinetics shows that as the Fe content increases, the incubation time of nucleation of the alloys decreases, and the nucleation is faster and easier. In addition, a large number of pre-existing crystal nuclei not only greatly reduces the nucleation activation energy of the alloy but also achieves grain refinement and excellent magnetic properties through grain competition growth.

Introduction

Fe-based nano-soft magnetic alloys stand out from traditional soft magnetic materials such as silicon steel and ferrite because of their saturation magnetic flux density (B_s), ultra-high permeability (μ_e), very low core loss (P) and close to zero saturation magnetostriction coefficient (λ_s), which promote them to play an indispensable role in the electronics industry [1, 2]. The FINEMET nanocrystalline alloys are gradually replacing energy-intensive traditional soft magnetic materials and further expanding the application fields [3–5]. In the face of miniaturization and

Handling Editor: Naiqin Zhao.

Address correspondence to E-mail: dongyq@nimte.ac.cn; qli@xju.edu.cn

https://doi.org/10.1007/s10853-021-05861-x

high-efficiency requirements, lower B_s of FINEMET alloys cannot fulfill market requirements [6]. In terms of optimizing B_s, researchers have conducted a lot of work, such as improving B_s via increasing Fe content [7, 8]. Nevertheless, as Fe content increases, the grains will be coarse easily, which leads to the rapid degradation of magnetic properties. In response to this situation, researchers have proposed a variety of strategies for composition design [9, 10] and heat treatment process [11]. For instance, Zhang W et al.[12] reported that FeSiBNbCu alloy with high Cu content has a large number of α-Fe nanoparticles in the quenched state, and nanocrystals with excellent properties can be prepared by heat treatment. In addition, various Cu clusters [10, 13] can also be prefabricated through two-step heat treatment processes [11, 14] to prepare nanocrystalline soft magnetic materials with excellent performance [15, 16]. The research of Professor A. Błachowicz on two-step annealing [17] illustrated that multitudinous Cu clusters could be prefabricated first and act as heterogeneous nucleation sites to reduce the activation energy of nucleation and promote the precipitation of new crystal nuclei. All crystal nuclei will grow up competitively [18] to refine the crystal grain size. Through the above method, the problems of the rapid coarsening of crystal grains and the rapid decline of magnetic properties during the annealing process can be effectively solved. Nevertheless, it is still a challenge and significant research to explore a more energy-efficient and simple annealing method to solve the above problems and develop high B_s FINEMET-like nanocrystalline alloys from composition design and heat treatment process.

In this study, we successfully design and prepare a series of FINEMET-like $Fe_{78}Si_{7.2}B_{13}Cu_{0.8}Nb_1$ (Fe78 alloy), $Fe_{80}Si_{6.2}B_{12}Cu_{0.8}Nb_1$ (Fe80 alloy) and $Fe_{82}Si_{5.2}B_{11}Cu_{0.8}Nb_1$ (Fe82 alloy) amorphous alloy ribbons with good surface quality and bending ductility. Two heat treatment methods are used to successfully prepare FINEMET-like nanocrystalline soft magnetic alloys with high Fe content, and a new preparation method for FINEMET-like nanocrystalline with high Fe content is successfully explored, that is, using a large number of pre-existing nuclei to reduce the activation energy of nucleation, generate a large number of nucleation sites, as well as nanocrystalline soft magnetic materials with excellent performance are prepared under the effect of the inhibition of the growth of large atoms and the competition mechanism between crystal grains.

Experimental

$Fe_{78+2x}Si_{7.2-x}B_{13-x}Cu_{0.8}Nb_1$ (x = 0, 1 and 2) master alloy ingots were smelted by induction-melting mixtures with high purity Fe (99.99%), Si (99.99%), B (99.95%), Cu (99.99%) and Nb (99.99%) in high-purity argon atmosphere and then were subject to melt-spinning technology to form amorphous alloy ribbons with a thickness of 22 μm and a width of 1.2 mm under a wheel velocity of 45 m/s. The onset crystallization temperature (T_x) was determined by a differential scanning calorimeter (DSC, NETZCH 404C) under the purity argon flow and the heating rate of 40 K/min. The structure characterization of melt-spun and annealed samples was examined by X-ray diffraction (XRD, D8 ADVANCE) with Cu-$K\alpha$ radiation and transmission electron microscopy (Tecnai F20). Nanocrystalline alloy ribbons were obtained by annealing melt-spun ribbons under vacuum atmosphere in a tube furnace and a rapid heating furnace, respectively. The coercivity (H_c) and saturation magnetic flux density (B_s) of the samples were measured by B-H loop tracer (EXPH-100) under a field of 800 A/m and vibrating sample magnetometer (VSM, Lakeshore7410) with a maximum field of 800 kA/m at room temperature, respectively. The permeability (μ) in the frequency range from 1 kHz to 110 MHz was examined by an impedance analyzer (Agilent 4294 A) in a field of 1 A/m.

Results and discussion

The melt-spun alloy ribbons of $Fe_{78+2x}Si_{7.2-x}B_{13-x}Cu_{0.8}Nb_1$ (x = 0, 1 and 2) with good surface quality and bending ductility were prepared by melt-spinning technique. The structure of free side of the as-spun alloy ribbons is identified by XRD, as shown in Fig. 1a, in which there is only a diffuse peak at around $2\theta = 45^\circ$ and no other obvious crystallization peaks, indicating that all the melt-spun ribbons are amorphous structures.

The thermal performances of the melt-spun ribbons were analyzed by DSC, as shown in Fig. 1b. The DSC curves of all the melt-spun alloy ribbons exhibit two obvious crystallization peaks with the onset

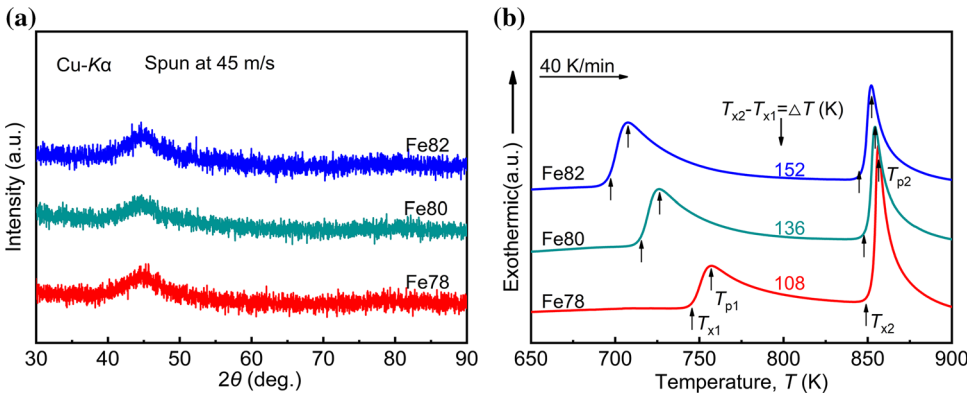

Figure 1 XRD patterns of free side (**a**) and DSC thermal scans measured at a heating rate of 40 K/min (**b**) of the as-spun alloy ribbons.

temperatures marked as T_{x1} and T_{x2}, and peak temperatures marked as T_{p1} and T_{p2}, respectively. According to the previous study [16], the first and second crystallization peaks correspond to the precipitation of α-Fe phase and compounds like boride, phosphide, etc., respectively. As the Fe content increases, the T_{x1} of the samples decreases monotonously and the T_{x2} is basically unchanged, leading to the widening of the temperature interval ΔT ($\Delta T = T_{x2}—T_{x1}$), which is 108 K, 136 K and 152 K for Fe78, Fe80 and Fe82 alloys, respectively. The larger ΔT will be favorable for controllable precipitation of α-Fe and will be conducive to form nanocrystalline alloy with a uniform "α-Fe + residual amorphous" structure through annealing treatment.

The changes of B_s, H_c and μ of the ribbon samples with the annealing temperature (T_A) are shown in Fig. 2 for CA and RA, respectively, in which CA refers to conventional annealing and RA refers to rapid annealing. The H_c change of the Fe82 alloy with T_A presents a typical "w" shape. A large amount of stress is produced in the as-spun ribbon due to rapid cooling. Stress pinning will affect the rotation of magnetic domains and thus lead to a large H_c. When the alloy is annealed at a low temperature, stress can be released and the H_c is reduced. When T_A further rises, a small amount of crystal grains begins to precipitate and coarsen rapidly in the alloy, which causes H_c to increase. When the T_A continues to rise, the alloy will enter nanocrystallization stage, in which a large number of uniform and dense nanocrystals are precipitated in the alloy and the grain size of the nanocrystals decreases with increasing T_A. Since the H_c depends on the grain size of nanocrystalline alloys [2], the H_c will gradually decrease with the increase in T_A in nanocrystallization stage, which corresponds to the lowest H_c. When T_A exceeds the optimum annealing temperature, the H_c will increase sharply due to the precipitation of boride [2, 3, 19]. The H_c of Fe78 and Fe80 alloys is not significantly reduced in the nanocrystallization stage, which may be due to the low nucleation rate of the alloys compared with Fe 82 alloy and does not precipitate dense and uniform nanocrystals during the annealing process. In addition, it can be found that the changing trend of H_c with T_A is just opposite to that of μ for all the alloys. This is because the factors causing the increase in H_c will also increase the difficulty of alloy magnetization, thereby reducing μ. It can be seen in Fig. 2 that, under the optimum annealing condition, RA can further optimize the magnetic properties of the Fe82 alloy compared with CA: H_c is reduced from 10.3 A/m to 5 A/m, and μ is increased from 19,000 to 20,000. This is because compared to CA, RA can form higher-density crystal nuclei and grow up. During the growth process, the growth time of a-Fe crystal grains is greatly shortened, the crystal grains are inhibited from coarsening, and the crystal grains keep the size uniform. At the same time, due to the high Fe content of Fe82 alloy, we believe there may be a certain number of pre-existing nuclei in the alloy due to the reduction of AFA. These nuclei compete with the new nucleation induced by Cu clusters to grow up, and RA faster heating rate can effectively inhibit the growth of pre-existing crystal nuclei and ensure synchronous growth with new crystal nuclei, thereby maintaining the uniformity of the nanocrystal size, which is unmatched by CA [18]. The essence of saturation magnetic flux density is the sum of the magnetic moments of the amorphous phase and the nanocrystalline phase. It can be seen in Fig. 2 that the value of B_s fluctuates slightly with the annealing temperature. Figure 3 is the B_s diagram of CA and

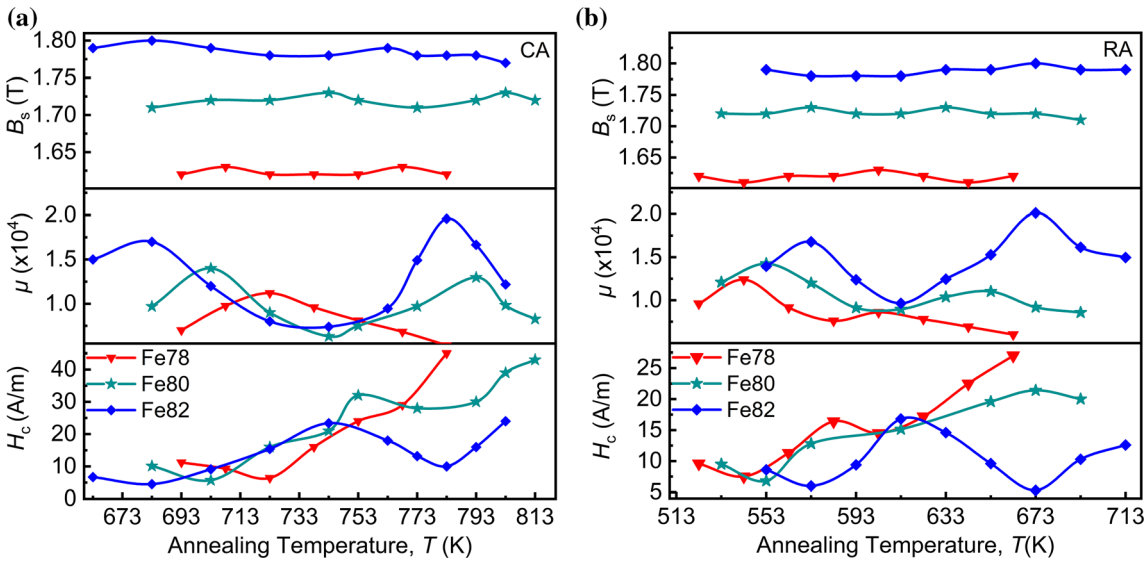

Figure 2 B_s, H_c and μ of the $Fe_{78+2x}Si_{7.2-x}B_{13-x}Cu_{0.8}Nb_1$ (x = 0, 1, 2) alloy ribbons annealed at different T_A by CA (**a**) and RA (**b**).

RA under optimal annealing conditions, and it can be seen that the B_s of the Fe82 alloy increases from 1.78 T for CA to 1.80 T for RA.

Exploration of the underlying mechanism of nanocrystallization

In order to further reveal the close relationship between magnetic properties and microstructure, the ribbon samples were observed by TEM. Figure 4a–c shows TEM bright field images with the corresponding selected area electron diffraction (SAED) patterns of the as-spun alloy ribbon of Fe78, Fe80 and Fe82, indicating that Fe78 and Fe80 alloys are typical amorphous structures while a large number of pre-existing nuclei with a size of about 3.5 nm can be found in amorphous matrix of Fe82 alloy. It is an interesting and significant topic whether excellent soft magnetic properties of the F82 alloy obtained by annealing treatment are closely related to these pre-existing nuclei. Therefore, we perform TEM observation on the samples and Fig. 5a–b shows TEM bright field image with the corresponding SAED pattern and grain size distribution for the F82 alloy ribbons annealed by CA and RA methods, respectively. The grains can be identified as α-Fe(Si) phase from the SAED patterns, which distribute evenly on amorphous matrix. It can be seen from TEM images that the average grain size of the F82 alloy ribbon after CA and RA is around 21.6 nm and 16 nm, respectively. The grain size is positively correlated with H_c, and it is indicated that RA can indeed an effective route to refine grains [20, 21, 23] and optimize soft magnetic properties of nanocrystalline alloys [22].

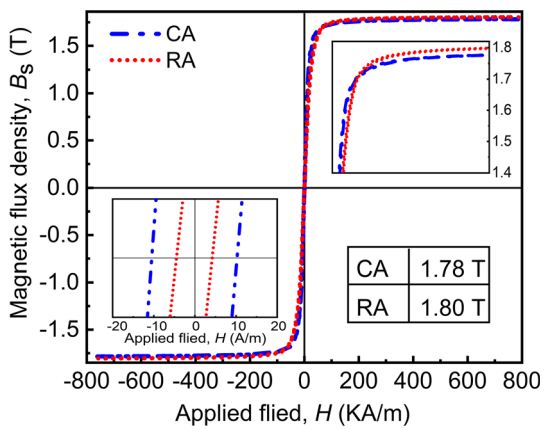

Figure 3 Hysteresis loop and B_s of the Fe82 alloy annealed by CA (783 K, 10 min) and RA (673 K, 5 min), respectively.

The crystallization kinetics of the present melt-spun ribbons is investigated using non-isothermal approach to explore the role of the pre-existing nuclei in the crystallization process. The effective activation energy, E, can be used to describe the difficulty of crystallization process and can be calculated using the Kissinger equation:

$$\ln\left(\frac{T^2}{\beta}\right) = \frac{E}{RT} + \text{constant} \quad (1)$$

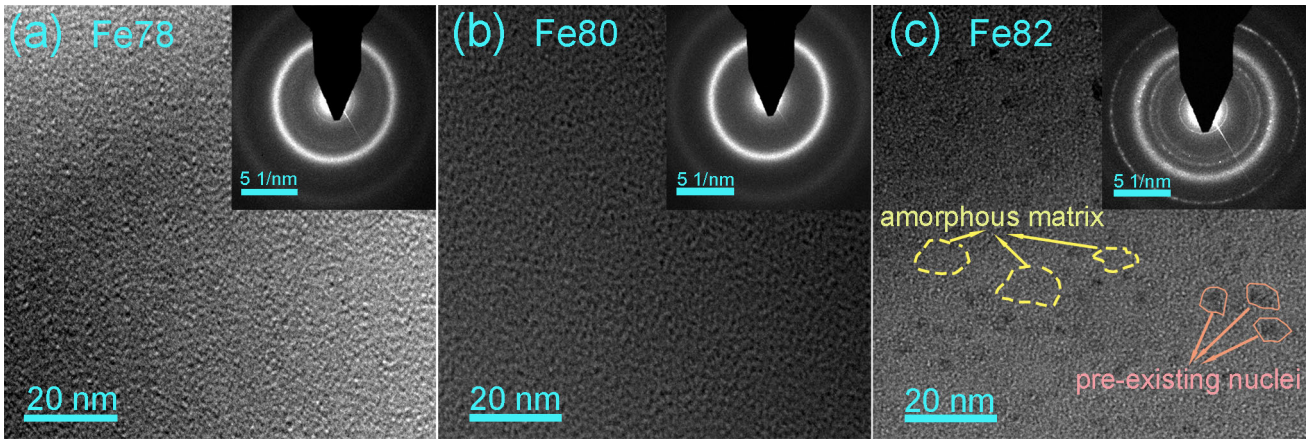

Figure 4 TEM bright field images with the corresponding selected area electron diffraction pattern from the middle layer of Fe78 (**a**), Fe80 (**b**), Fe82 (**c**) melt-spun ribbon samples.

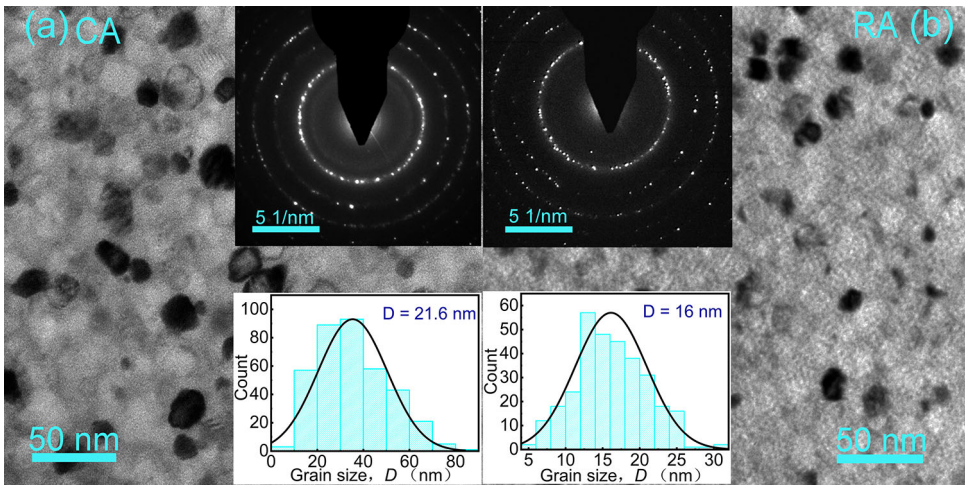

Figure 5 TEM bright field images with the corresponding selected area electron diffraction patterns and grain size distribution for the Fe82 alloy ribbons obtained by CA (**a**) and RA (**b**).

where R = 8.314 J/(mol·K) is the universal gas constant; β is the heating rate during continuous heating; T is the characteristic temperature, and when the characteristic temperature is taken as the initial temperature (T_x) and the peak temperature (T_p) of crystallization peak, the corresponding effective activation energy is referred to E_x and E_p, respectively. By plotting $\ln(T^2/\beta)$ as a function of $1000/T$, a linear dependence with the slope of E/R can be obtained as presented in Fig. 6a. From this slope, the activation energy for each characteristic event was calculated and the data are drawn in Fig. 6b. The E_x and E_p can directly reflect the difficulty for nucleation and growth of crystal grains in a crystallization process, respectively [24]. The E_{x1}, E_{p1}, E_{x2} and E_{p2} of the as-spun $Fe_{78+2x}Si_{7.2-x}B_{13-x}Cu_{0.8}Nb_1$ alloy ribbons can be determined by Kissinger method and are presented in Fig. 6b. Based on the DSC analysis, the E_{x1} and E_{x2} correspond to the activation energy for the nucleation of α-Fe and compounds like boride, phosphide etc., respectively. It can be seen that the E_{x2} is much larger than E_{x1}, which may be because the pre-existing α-Fe nuclei and gradually decreasing AFA reduce the nucleation activation energy and promote the precipitation of α-Fe phase easier. Additionally, the E_{x1} gradually decreases with the increase in Fe content, indicating that the number of the existing pre-existing α-Fe nuclei increases with the Fe content. The result is consistent with that observed by TEM as shown in Fig. 4c.

For DSC trace measured in isochronal mode, the crystallized volume fraction at the temperature of T, $\alpha(T)$, for a crystallization process can be expressed by the following formula [25]:

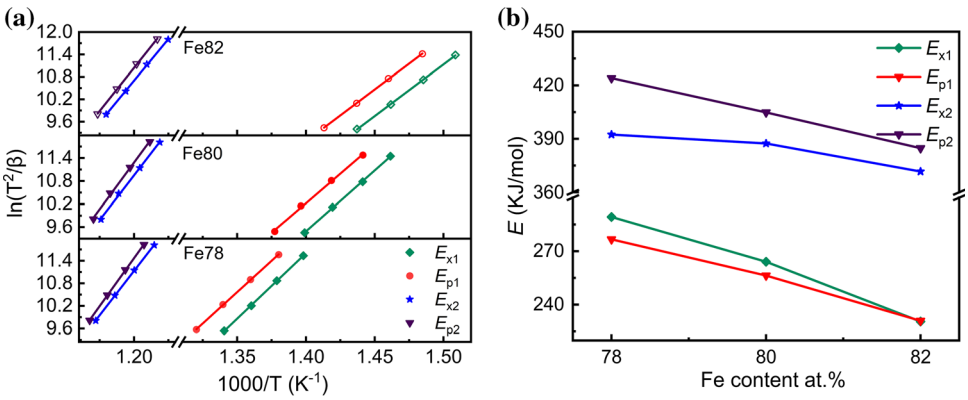

Figure 6 Kissinger plots for the T_{x1}, T_{p1}, T_{x2} and T_{p2} (**a**) and the changes of the activation energy of the E_{x1}, E_{p1}, E_{x2} and E_{p2} determined from Kissinger plots with the alloy composition (**b**) of the as-spun $Fe_{78+2x}Si_{7.2-x}B_{13-x}Cu_{0.8}Nb_1$ (x = 0, 1, 2) alloy ribbons.

$$\alpha(T) = \frac{\int_{T_0}^{T}(dH/dT)}{\int_{T_0}^{T}(dH/dT)} = \frac{A_T}{A} \tag{2}$$

where T_∞ is the end crystallization temperature; dH/dT is the heat capacity at atmospheric pressure; A_T and A are the areas of crystallization peak in the isochronal DSC trace from T_0 and T to T_∞, respectively. The crystallized volume fraction is plotted as a function of temperature as shown in Fig. 7a. Obviously, the plots of $\alpha(T)$ for the first crystallization peak in the DSC trace of the alloys ribbons at the heating rate of 20 K/min follow a sigmoidal behavior, and its slope represents the crystallization rate under a constant heating rate [26]. As shown in Fig. 7a, the slop of $\alpha(T)$ curve, i.e., crystallization rate, of Fe82 alloy is less than that of Fe78 and Fe80 alloys, indicating that the crystallized volume fraction α is about 0.2 to 0.8, the crystallization rate is greater, and with the increase in Fe content, the incubation time of nucleation decreases, indicating a larger growth resistance of α-Fe grains in Fe82 alloy, which is conducive to the formation of fine nanocrystalline structure. Additionally, it can be found in Fig. 7a that, with the increase in Fe content, the incubation time of nucleation of the alloys decreases, i.e., the nucleation is faster and easier. This may be because there are more pre-existing α-Fe nuclei in the as-spun alloy ribbons with the increase in Fe content, which greatly reduces the activation energy of nucleation and leads to a short incubation time of nucleation.

In order to analyze the crystallization mechanism, local Avrami exponent (n) for the crystallization process is evolved by Blázquez method. The plots of ln[-ln(1-α)] versus ln[(T–T_0)/β] are presented in Fig. 7b. For non-isothermal processes, n can be calculated by the modified JMAK equation [25]:

$$n(\alpha) = \frac{1}{1+\frac{E}{RT}\left(1-\frac{T_0}{T}\right)} \frac{d\{\ln[-\ln(1-\alpha)]\}}{d\left[\ln\left(\frac{T-T_0}{\beta}\right)\right]} \tag{3}$$

where T_0 is the onset temperature of crystallization, β is the heating rate and E is the activation energy. The Avrami exponent, n, involves the information about the nucleation and growth mechanism in the crystallization process and is related to a (the nucleation index), b (the dimensionality of growth) and p (the growth index) as the following equation [27–31]:

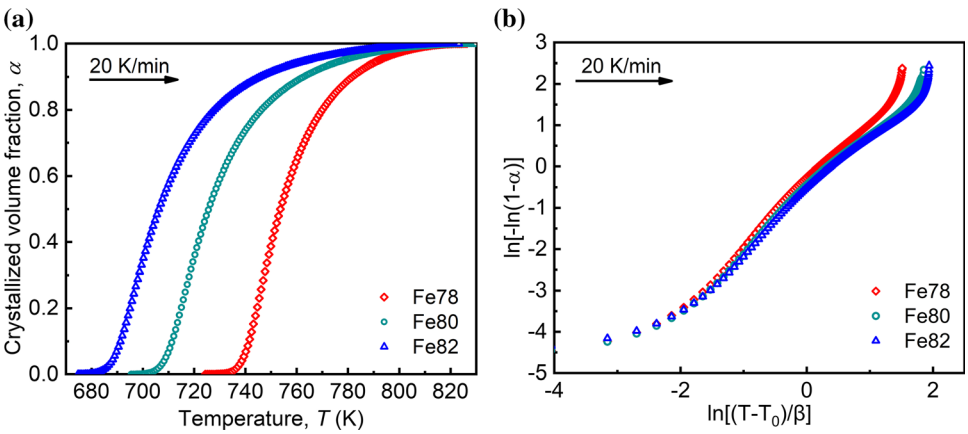

Figure 7 Curves of crystallization volume fraction versus temperature T for the first crystallization peak of the alloys ribbon at different heating rates (**a**) and plots of ln[-ln(1-α)] versus ln[(T–T_0)/β] (**b**).

$$n = a + bp \quad (4)$$

where a is the nucleation index, and a = 0, $0 < a < 1$, $a = 1$ and $a > 1$ correspond to zero nucleation rate, nucleation rate decreasing with time, constant nucleation rate and nucleation rate increasing with time, respectively. b is the dimension index of growth, and $b = 1$, 2 and 3 that correspond to one-dimensional, two-dimensional and three-dimensional growth, respectively. p is the growth index, and $p = 0.5$ and 1 correspond to diffusion-controlled growth and interface controlled growth, respectively. The different mechanism of nucleation and growth in the crystallization process corresponds to different values of a, b and p, thus different value of n. Many researchers reported that the growth of Fe-based amorphous alloys is controlled by diffusion and thus $p = 0.5$ here [25, 30–32]. Further provided that the precipitation of the present crystalline phase follows a three-dimensional growth. Therefore, $n < 1.5$ reflects the crystallization process of the direct growth of pre-existing crystal nuclei; $1.5 < n < 2.5$ reflects the crystallization process of the growth with decreasing nucleation rate; $n > 2.5$ represents the growth with increasing nucleation rate.

As shown in Fig. 8, the n value of all the three alloys for the first crystallization peak at a heating rate of 20 K/min is in the range of 1.2–2, when $0.2 < \alpha < 0.8$. Taking Fe82 alloy as an example, when $\alpha < 0.38$, $1.5 < n < 2$, meaning the crystallization mechanism of the growth with decreasing nucleation rate along with a certain number of pre-existing nuclei. When crystallization volume fraction $\alpha > 0.38$, $n < 1.5$, reflecting the crystallization mechanism of the direct growth of pre-existing crystal nuclei, which

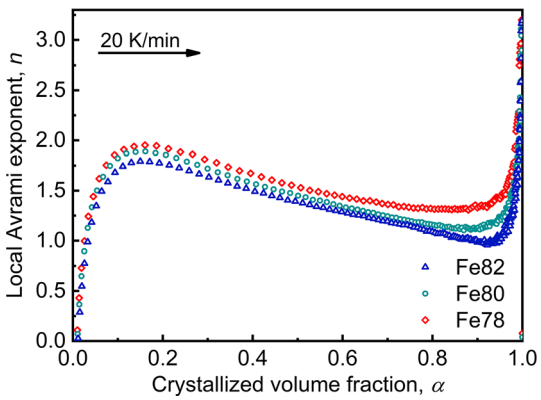

Figure 8 Local Avrami exponent, n, as a function of crystallized volume fraction for the first crystallzation peak of the alloys.

may be explained in the following two reasons: (1) As the crystallization fraction increases, there is no space enough for nucleation, which causes the nucleation index, a, to tend to 0; (2) As the crystallization fraction increases, the growth dimension of the crystal grains in the ribbon samples is restricted, which leads to the decrease in the dimension index of growth, b. Additionally, it can be seen in Fig. 8 that the n value of Fe78, Fe80 and Fe82 alloys decrease in turn in the whole crystallization process, indicating again that the number of the pre-existing α-Fe nuclei in the as-spun alloys increases with the Fe content.

Conclusions

In this work, high B_s FINEMET-like nanocrystalline alloy of $Fe_{82}Si_{5.2}B_{11}Cu_{0.8}Nb_1$ is obtained by annealing the corresponding melt-spun alloy ribbons with high-density pre-existing nuclei, as well as the magnetic properties and microstructure of the resultant nanocrystalline alloy is thoroughly studied. The obtained results are as follows:

1. $Fe_{82}Si_{5.2}B_{11}Cu_{0.8}Nb_1$ melt-spun amorphous ribbon with high Fe content and the wide heat treatment window ΔT of over 150 K has been prepared successfully.
2. The $Fe_{82}Si_{5.2}B_{11}Cu_{0.8}Nb_1$ nanocrystalline alloy can be prepared through CA and RA, and the resultant nanocrystalline alloy, in which α-Fe nanograin with an average grain size of 16 nm buried in amorphous matrix, exhibits high B_s of 1.80 T, low H_c of 5 A/m and high μ of 20,000 at 1 kHz. Such the excellent magnetic properties may stem from the numerous pre-existing α-Fe nuclei in the as-spun amorphous ribbons.
3. It is found that the active energy for α-Fe nucleation decreases with the increase in Fe content and exist a large number of pre-existing α-Fe nuclei in the as-spun Fe82 ribbon, which provides a solid foundation for grain refinement through competitive growth.

Acknowledgments

This work was supported by the National Key Research and Development Program of China (grant number 2016YFB0300500), the S&T Innovation 2025

Major Special Program (grant number 2018B10084), the National Natural Science Foundation of China (grant number 51801224, 51771161), and the Leading Talents of Tianshan Cedar Program of Xinjiang Uygur Autonomous Region (grant number 2019XS02) and the Tianshan Innovation Team Program of Xinjiang Uygur Autonomous Region (grand number 2020D14038).

References

[1] Gutfleisch O, Willard MA, Brück E, Christina H, Chen SG, Sankar LPJ (2011) Magnetic materials and devices for the 21st century: stronger, lighter, and more energy efficient. Adv Mater 23:821–842. https://doi.org/10.1016/S0921-5093(96)10693-6

[2] Herzer G (2013) Modern soft magnets: amorphous and nanocrystalline materials. Acta Mater 61:718–734. https://doi.org/10.1016/j.actamat.2012.10.040

[3] Zhao CL, Wang AD, He AN, Yue SQ, Chang CT, Wang XM, Li RW (2016) Correlation between soft-magnetic properties and T_{x1}-T_c in high B_s FeCoSiBPC amorphous alloys. J Alloy Compd 659:193–197. https://doi.org/10.1016/j.jallcom.2015.11.044

[4] Azuma D, Hasegawa R (2008) Audible noise from amorphous metal and silicon steel-based transformer core. IEEE Trans Magn 44:4104–4106. https://doi.org/10.1109/TMAG.2008.2003174

[5] Wang AD, Zhao CL, Men H, He AN, Chang CT, Wang XM, Li RW (2015) Fe-based amorphous alloys for wide ribbon production with high B_s and outstanding amorphous forming ability. J Alloy Compd 630:209–213. https://doi.org/10.1016/j.jallcom.2015.01.056

[6] Yoshizawa Y, Oguma S, Yamauchi K (1988) New Fe-based soft magnetic alloys composed of ultrafine grain structure. J Appl Phys 64:6044–6046. https://doi.org/10.1063/1.342149

[7] Makino A, Men H, Kubota T, Yubuta K, Inoue A (2009) New excellent soft magnetic FeSiBPCu nanocrystallized alloys with high B_s of 1.9 T from nanohetero-amorphous phase. IEEE Trans Magn 45:4302–4305. https://doi.org/10.1109/TMAG.2009.2023862

[8] Makino A, Men A, Kubota T, Yubuta K, Inoue A (2009) New Fe-metalloids based nanocrystalline alloys with high B_s of 1.9 T and excellent magnetic softness. J Appl Phys 105:218–221. https://doi.org/10.1063/1.3058624

[9] Liu T, Wang AD, Zhao CL, Yue SQ, Wang XM, Liu CT (2019) Compositional design and crystallization mechanism of High B_s nanocrystalline alloys. Mater Res Bull 112:323–330. https://doi.org/10.1016/j.materresbull.2019.01.007

[10] Ren XC, Li YH, Jia XJ, Qiu ZY, Xie GY, Zhang W (2018) Microstructure and magnetic properties of $Fe_{81.3}Si_4B_{13}Cu_{1.7}$ nanocrystalline alloys with minor Nb addition. J Iron Steel Res Int 25:614–618. https://doi.org/10.1007/s42243-018-0087-2

[11] Motoki O, Yoshihito Y (2009) Effect of heating rate on soft magnetic properties in nanocrystalline $Fe_{80.5}Cu_{1.5}Si_4B_{14}$ and $Fe_{82}Cu_1Nb_1Si_4B_{12}$ alloys. Appl Phys Express 023005. https://doi.org/10.1143/APEX.2.023005

[12] Li YH, Jia XJ, Zhang W, Zhang Y, Xie GY, Qiu ZY, Luan JH, Jiao ZB (2021) Formation and crystallization behavior of Fe-based amorphous precursors with pre-existing α-Fe nanoparticles—Structure and magnetic properties of high-Cu-content Fe-Si-B-Cu-Nb nanocrystalline alloys. J Mater Sci Technol 65:171–181. https://doi.org/10.1016/j.jmst.2020.05.049

[13] Motoki O, Yoshihito Y (2008) Cu addition effect on soft magnetic properties in FeSiB alloy system. J Appl Phys 103:07E722. https://doi.org/10.1063/1.2829240

[14] Zang B, Parsons R, Onodera K, Kishimoto H, Kato A, Liu ACY, Suzuki K (2017) Effect of heating rate during primary crystallization on soft magnetic properties of melt-spun FeB alloys. Scripta Mater 132:68–72. https://doi.org/10.1016/j.scriptamat.2017.01.030

[15] Suzuki K, Parsons R, Zang BW, Onodera K, Kishimoto H, Kato A (2017) Copper-free nanocrystalline soft magnetic materials with high saturation magnetization comparable to that of Si steel. Appl Phys Lett 110:012407–012414. https://doi.org/10.1063/1.4973772

[16] Han YB, Wang AD, He AN, Chang CT, Li FS, Wang XM (2015) Improvement of magnetic properties, microstructure and magnetic structure of $Fe_{73.5}Cu_1Nb_3Si_{15.5}B_7$ nanocrystalline alloys by two-step annealing process. J Mater Sci Mater Electron 27:3736–3741. https://doi.org/10.1007/s10854-015-4216-4

[17] Gupta P, Gupta A, Shukla A, Ganguli T, Sinha AK (2011) Structural evolution and the kinetics of Cu clustering in the amorphous phase of Fe-Cu-Nb-Si-B alloy. J Appl Phys 110:033537. https://doi.org/10.1063/1.3622325

[18] Sharma P, Zhang X, Zhang Y, Makinoa A (2015) Competition driven nanocrystallization in high B_s and low coreloss FeSiBPCu soft magnetic alloys. Scripta Mater 95:3–6. https://doi.org/10.1016/j.scriptamat.2014.08.023

[19] Bitoha T, Makinoa A, Inoueb A, Masumoto T (2003) Random Anisotropy Model for nanocrystalline soft magnetic alloys with grain-size distribution. Mater Trans 44:2011–2019. https://doi.org/10.2320/matertrans.44.2011

[20] Bitoha T, Makinoa A, Inoueb A (2004) The effect of grain-size distribution on coercivity in nanocrystalline soft magnetic alloys. J Magn Magn Mater 272:1445–1446. https://doi.org/10.1016/j.jmmm.2003.12.368

[21] Yashpal SV, Kumar BVM (2015) Issues in determining size of nano-crystalline ceramic particles by X-ray diffusion. Mater Today 2:3534–3538. https://doi.org/10.1016/j.matpr.2015.07.330

[22] Parsonsa R, Zang B, Onoderab K, Kishimotob H, Shojib T (2019) Core loss of ultra-rapidly annealed Fe-rich nanocrystalline soft magnetic alloys. J Magn Magn Mater 476:142–148. https://doi.org/10.1016/j.jmmm.2018.12.053

[23] Suzuki K, Ito N, Garitaonandia JS, Cashion JD, Herzer G (2008) Local random magnetocrystalline and macroscopic induced anisotropies in magnetic nanostructures. J Non-Cryst Solids 354:5089–5092. https://doi.org/10.1016/j.jnoncrysol.2008.06.118

[24] Lin WD, Yang YZ, Xu J, Li W (2018) Effect of Nb, Si and Cu on the crystallization process and magnetic properties of FeNbBP alloys. J Alloy Compd 735:1195–1199. https://doi.org/10.1016/j.jallcom.2017.11.256

[25] Ramasamy P, Stoica M, Taghvaei A, Prashanth KG, Kumar R, Eckert J (2016) Kinetic analysis of the non-isothermal crystallization process, magnetic and mechanical properties of FeCoBSiNb and FeCoBSiNbCu bulk metallic glasses. J Appl Phys 119:073908. https://doi.org/10.1063/1.4942179

[26] Jerzy A, Marcin K, Elżbieta J, Jerzy L (2009) Small-angle X-ray scattering from phase-separating amorphous metallic Alloys undergoing nanocrystallization. J Alloy Compd 483:116–119. https://doi.org/10.1016/j.jallcom.2008.08.117

[27] Arun P, Lad KN, Rao TSL, Pinal M (2004) Kinetics of crystallization of amorphous $Cu_{50}Ti_{50}$ alloy. J Non-Cryst Solids 345:178–181. https://doi.org/10.1016/j.jnoncrysol.2004.08.018

[28] Ashish S, Shravana K, JaN I, Dahotre NB (2013) Nanocrystallization in spark plasma sintered $Fe_{48}Cr_{15}Mo_{14}$-$Y_2C_{15}B_6$ bulk amorphous alloy. J Appl Phys 114:054903. https://doi.org/10.1063/1.4817379

[29] Pere B, Rojas PE, Jose I, Daniel C (2009) Phase-field modelling of microstructural evolution in primary crystallization. J Alloy Compd 483:645–649. https://doi.org/10.1016/j.jallcom.2008.07.215

[30] Peng C, Chen ZH, Zhao XY, Zhang AL, Zhang LK, Chen D (2014) Crystallization kinetics of $Zr_{60}Cu_{25}Fe_5Al_{10}$ bulk metallic glass. J Non-Cryst Solids 405:7–11. https://doi.org/10.1016/j.jnoncrysol.2014.08.030

[31] Ouyang YF, Wang LY, Chen HM, Cheng XY (2008) The formation and crystallization of amorphous $Al_{65}Fe_{20}Zr_{15}$. J Non-Cryst Solids 354:5555–5558. https://doi.org/10.1016/j.jnoncrysol.2007.02.099

[32] Wang Y, Xu K, Li Q (2012) Comparative study of non-isothermal crystallization kinetics between $Fe_{80}P_{13}C_7$ bulk metallic glass and melt-spun glassy ribbon. J Alloy Compd 540:6–15. https://doi.org/10.1016/j.jallcom.2012.06.016